Applied Catalysis A, General 643 (2022) 118786

Contents lists available at ScienceDirect

Applied Catalysis A, General

journal homepage: www.elsevier.com/locate/apcata

Activity of carbon-encapsulated $Ni_{12-x}Fe_xP_5$ catalysts for the oxygen evolution reaction: Combination of high activity and stability

Fatemeh Poureshghi [a,1], Frode Seland [a], Jens Oluf Jensen [b], Svein Sunde [a,*]

[a] Department of Materials Science and Engineering, Norwegian University of Science and Technology (NTNU), N-7491Trondheim, Norway
[b] Department of Energy Conversion and Storage, Technical University of Denmark, DK-2800 Kgs. Lyngby, Denmark

ARTICLE INFO

Keywords:
Water electrolysis
Oxygen evolution reaction
Nickel-iron phosphide
Carbon encapsulation

ABSTRACT

Rational design of efficient, earth-abundant, and durable electrocatalysts to accelerate the oxygen evolution reaction (OER) is critical for hydrogen ion by water electrolysis. In the present work, nanostructured $Ni_{12-x}Fe_xP_5$ ($x = 1.2, 2.4, 3.6$) OER electrocatalysts synthesized by a colloidal method is reported. For $x = 1.2$, an alloy of Ni, Fe, and P is formed. For $x = 2.4$ or $x = 3.6$, a core-shell NiFeP@Fe_3O_4 structure is formed. The nanoparticles are encapsulated in a self-generated carbon layer. The carbon layer is formed during synthesis from synthesis residues. The carbon-encapsulated $Ni_{9.6}Fe_{2.4}P_5$ catalyst offers the outstanding mass activity of 0.1 A mg^{-1} and overpotential of 220 mV at 10 mA cm^{-2}, assigned to a combination of enhanced electrical conductivity provided by the carbon shell, a large surface area, and a high specific catalytic activity. Post-mortem characterization indicates that the carbon encapsulation remains intact under conditions of the OER.

1. Introduction

Water splitting by electrolysis ($2H_2O \rightarrow O_2 + 2H_2$) provides a possible path for the conversion of clean, renewable energy to H_2 fuel to power human civilization [1,2]. The efficiency of water electrolysis is partially limited by the high kinetic overpotential associated with driving the oxygen evolution reaction (OER) [1,3,4]. Therefore, development of efficient catalysts is indispensable to facilitate fast kinetics (i.e. low overpotential). An ideal OER catalyst would be composed of nontoxic earth-abundant elements, economical to manufacture, chemically and mechanically stable, and sufficiently electrically conductive [5–7].

Development of improved catalysts can be accelerated by an enhanced understanding of the underlying electrocatalytic mechanism and its dependence on catalyst composition and structure. The paradigm for understanding heterogeneous OER catalysis that has emerged over a century of research is based on the application of the Sabatier principle. The OER occurs on the catalyst surface sites, M, via a series of intermediates (e.g. M-OH, M-O, M-OOH, M-OO) [3]. If all of the intermediates are bound by an M-O bond, plotting activity versus the M-O bond strength should, in principle, result in a volcano-shaped graph, i.e a so-called "volcano plot". At either side of the apex of the volcano the bond strength is sub-optimal; surfaces with either too large or too small M-O bond strengths are poor catalysts, as both lead to rate-determining steps with free energies that are larger than the average free energy for the steps in the mechanism [3]. OER catalysts based on earth-abundant first-row transition metals is of particular interest, as these catalysts might be used in water electrolysis or photoelectrolysis systems at a scale commensurate with global energy use. Consequently, there have been many experimental and computational efforts to correlate OER activity to chemical or material parameters. Mn [8], Fe [9], Co [10], and Ni-based [11] metal oxides and (oxy)hydroxides have been broadly studied and benchmarked for OER catalysis.

Ni and its bimetallic oxides, particularly with Fe, are state-of-the-art catalysts in alkaline medium [12–15]; a $Ni_{0.9}Fe_{0.1}O_x$ OER activity was reported to surpass that of IrO_2 [11]. Early studies by Corrigan and co-workers [16,17] and more recent ones by Boettcher et al. [18] show that Fe impurities from the electrolyte are readily incorporated into the $Ni(OH)_2$ and significantly enhance the activity, but the role of Fe is still being debated. While various types of NiFe with alloys have been reported [14], Cui et al. [19] reported that a porous monolithic NiFe structure prepared by dealloying NiFeAl alloy exhibited much higher OER activity than the NiFe alloy itself. The improved performance was attributed to a large number of active sites and fast electron/mass

* Corresponding author.
E-mail address: svein.sunde@material.ntnu.no (S. Sunde).
[1] Current address: Department of Building, Energy and Material Technology, UiT- The Arctic University of Norway, N-8514 Narvik, Norway.

https://doi.org/10.1016/j.apcata.2022.118786
Received 30 May 2022; Received in revised form 14 July 2022; Accepted 15 July 2022
Available online 19 July 2022

transfer induced by the porous structure.

Despite the high activity of some metal oxides, reported so far, most metal oxides possess insufficient electric conductivity for electrocatalytic purposes, as a low conductivity impedes the electron transport inside the bulk of the catalysts and between neighbouring catalyst nanoparticles (NPs), compromising kinetics [20]. However, Stevens et al. [21] concluded that in case of electrodeposited thin layers, conductivity enhancements does not necessarily enhance the electrocatalytic activity. Moreover, transition-metal-oxide/transition-metal nanocomposites such as NiO/Ni, FeO/Fe, and CoO/Co are inherently magnetic, the magnetic properties varying with size, crystal structure, and morphology, thus showing a wide variety of intriguing phenomena [22,23]. In the present context, the main issue concerning magnetism is that it may adversely affect colloidal stability and lead to particle agglomeration. This, in turn, decreases the active surface area and consequently leads to lower catalytic activity [24,25]. However, it should be noted that the decrease in activity due to magnetism might not be palpable when the catalysts are prepared via electrodeposition or formed on a porous support [26] as the agglomeration happens just in the powder form, and not an issue when they are prepared on a substrate. Therefore, optimizing the electrical behavior of the transition metal oxides or hydroxides and enhancing their colloidal stability to maintain the desired high specific surface area are two main properties that need to be considered in designing efficient catalysts. In order to overcome the aforementioned issues, conductive additives, such as carbon, have been extensively used to support transition metals and semiconducting or insulating metal oxide nanoparticles [27,28]. However, corrosion of carbon materials under OER conditions is under debate, and the absence of a solution to this problem prevents the industry from considering them as additives or supports for anodes in water electrolysis systems. Moreover, anodic degradation of carbon materials may not only decrease the extent of metal oxide utilization during the OER, but also leads to an uncertainty in the determination of the OER activity if the corrosion contribution to the oxidation current is not considered explicitly [29–31].

In this context, transition metal phosphides (TMPs) [32] and carbon-encapsulated materials [33,34] have been reported as promising candidates for efficient electrocatalysis with enhanced activity compared with transition metal or metal oxides, which can be ascribed to both their nonmagnetic nature [35] (which translates to higher active surface area), and optimizing the electron transport inside the bulk of the electrocatalyst [36]. Among, all the tested transition metal-based catalysts, TMPs have the lowest overpotentials demonstrated to date [37]. A number of studies show that TMPs undergo an in situ electrochemical transformation under anodic oxidation conditions, being irreversibly converted to transition metal (oxy)hydroxides (TMOHs). These TMHOs have been proposed to be the true catalytically active species for the OER [38]. On the other hand, no such transformation was observed in TMP electrocatalysts after the OER by Liu et al. [39] and Liang et al. [40]. In this respect, TMPs are mainly considered as "pre--catalysts", i.e. a catalyst that transforms into the actual catalytic material under and as a consequence of the operating conditions, rather than "catalysts" that maintains its nascent structure under any relevant conditions [32,38].

Interestingly, there are many reports showing that the electrocatalytic activity of TMPs is enhanced by in situ formation of TMHOs on the surface. In other words, TMHOs-TMP composites formed in situ exhibit a better apparent OER performance than the corresponding pristine TMOs or TMHOs synthesized directly [41,42]. Although the underlying mechanisms are not fully understood, many studies have provided clues that the electrochemical oxidation of TMPs would enable the exposure of high density catalytically active sites. Moreover, any TMP with superior conductivity underneath a TMHO surface layers would facilitate electron transfer at the interface as well as electron transport inside the bulk component [43,44]. In the past few years, large research efforts have been devoted towards developing various TMP pre-catalysts for use in catalyzing the OER.

The concept of encapsulating nanoparticles of non-precious 3*d* TMs and their alloys in various carbon matrices as an alternative towards efficient catalysts for the OER, ORR, and HER has recently attracted substantial attention [34,45,46]. Depending on the purpose, the carbon shell in carbon encapsulated nanoparticles plays different roles or provide multi-functionality. For instance, carbon encapsulated Pt nanoparticles in which Pt is electrochemically active show high durability as a result of a protection provided by the carbon shell. On the other hand, the electronic properties of the carbon shell can be modulated by the metallic nanoparticle cores, allowing for the binding energies of reaction intermediates on the carbon surface to be tuned. In some cases, carbon encapsulated metal nanoparticles exhibit high activity simultaneously against a variety of electrochemical reactions (e.g., HER and OER), demonstrating a bi-functional catalyst [47–49].

Different methods, such as chemical vapor deposition (CVD), the polymer coating method, the solvothermal method, and the high-temperature pyrolytic method, have been utilized to form a thin carbon shell to encapsulate metal nanoparticles. Among all these, the solvothermal method has been given the most interest due to several advantages including a low temperature process ($< 300\ ^{\circ}C$), morphology tuning, time-efficient, possible scale-up, possibility of engineering the carbon shell, and so forth [47].

For the first time, Carenco *et al.* [50] reported synthesis of carbon-encapsulated Ni_2P nanoparticles via a solvothermal method, in which amorphous Ni_2P nanoparticles were synthesized with excess amount of trioctylphosphine (TOP) at 220 °C and then subsequently converted to carbon-encapsulated nanoparticles by heating in a Schlenk tube for 30 min at 400 °C, under N_2. The carbon layer was formed due to the decomposition of an excess amount of TOP during an annealing procedure.

Recently, Jung and co-workers [47,51] have reported the synthesis of various transition metal nanoparticles encapsulated by carbon shell through the solvothermal method, which involves decomposing metal acetylacetonates precursors in organic solvents with surfactants under inert atmospheres at temperatures below 300 °C, after which the products are processed and subjected to annealing under different gas conditions to yield different carbon encapsulated metal structures. The carbon layer formed through the annealing step, in which the carbon atoms absorbed inside the lattice of the metal alloys diffuse to the nanoparticle surface, producing a mono or bilayer-level uniform carbon shell at the sub-nm scale.

In the present work, we report the fabrication of ternary $Ni_{12-x}Fe_xP_5$ nanoparticles ($x = 0$, 1.2, 2.4, 3.6) via a colloidal synthesis route. By introducing Fe precursors to the synthetic solution, a self-generated carbon layer surrounds the particles as the native ligand covering the nanoparticles is decomposed and lead to the formation of a carbon layer. This is contingent on the decomposition of the precursors happening at a high enough temperature, 300 °C in this work, and which is possibly catalyzed by the Ni-Fe bimetallic system. The key aspect of this catalyst design is that the carbon layer can provide a large specific area and interconnected electrically conducting networks which promotes the electrocatalytic activity of NiFeP nanoparticles significantly. Moreover, the stability of the carbon layer and NiFeP catalyst after being subjected to OER conditions were evaluated by TEM and Raman spectroscopy.

2. Experimental

2.1. Materials

Oleylamine (OAm; technical grade, 70 %), tri-n-octylphosphine (TOP; 97 %), nickel(II) acetylacetonate ($Ni(acac)_2$; 97 %), iron(III) acetylacetonate ($Fe(acac)_3$; anhydrous, 95 %), toluene (anhydrous, 99.8 %), acetone (99.5 %), isopropanol (IPA; 99.5 %), potassium hydroxide (99.99 %), and (5 wt%) Nafion 117 solution. All chemicals were purchased from Sigma-Aldrich and used as received, without further

purification.

Deionized water (DI-water), generated by a Milli-Q water system 18.2 MΩ cm^{-1}, was used for all measurements.

2.2. Synthesis of ternary $Ni_{12-x}Fe_xP_5$ nanocrystallites ($0 \leq x < 1$)

For all the catalysts in this work, the entire synthesis was completed in a single reactor in a dry, oxygen-free, Ar atmosphere (99.9999 %) by the use of Schlenk lines and a glove box. The protocol developed to synthesize $Ni_{12-x}Fe_xP_5$ nanoparticles is based on the method refined by Muthuswamy et al. [52] to synthesize discrete $Ni_{12}P_5$ phase-pure nanoparticles.

Formation of $Ni_{12}P_5$ and nickel-iron phosphide nanoparticles was achieved by reaction of $Ni(acac)_2$ or mixtures of $Ni(acac)_2$ and $Fe(acac)_3$, respectively, with TOP as the P source in the presence of oleylamine via a two-step process. The two-step procedure is comprised of the generation of Ni and Ni_xFe_{1-x} precursor particles at 220 °C followed by further reaction and crystallization at 300 °C. In a typical synthesis, 50 mL of OAm (156 mmol) was added to a 250 mL three-neck round bottom flask and evacuated for 10 min at room temperature. In the next step the corresponding amount (overall 15.6 mmol) of the two metal precursors ($Ni(acac)_2$ and $Fe(acac)_3$) (Fe:Ni molar ratios were 0.1, 0.2, or 0.3), and 14 mL TOP (31.2 mmol) were added to the solution and kept at 50 °C (ramp rate of $3\,^{\circ}C\,min^{-1}$) for 5 min under Ar atmosphere (99.9999 %). Then the temperature was ramped to 220 °C at rate of $8\,^{\circ}C\,min^{-1}$ and kept at this temperature for 2 h. In the second step the flask was heated further until 300 °C and kept for 30 min at this temperature. Once the reaction had finished, the flask was left to cool to room temperature either gradually while it was kept inside the heating mantle or with the heating mantle removed immediately after synthesis. The nanoparticles were isolated and washed at least three times using a mixture of isopropanol, toluene, and acetone to remove the remaining reagents and organic matter. Black powder (1.2 g) was obtained, which corresponds to a 100 % yield of $Ni_{12-x}Fe_xP_5$ nanoparticles.

We will designate the $Ni_{12-x}Fe_xP_5$ compositions as $Ni_{10.8}Fe_{1.2}P_5$ for $x = 1.2$, $Ni_{9.6}Fe_{2.4}P_5$ for $x = 2.4$, and $Ni_{8.4}Fe_{3.6}P_5$ for $x = 3.6$ below.

2.3. X-ray powder diffraction and Rietveld refinement

Powder X-ray diffraction (PXRD) was carried out on a Bruker D8 DaVinci X-ray Diffractometer with Cu Kα radiation (Billerica, Massachusetts, USA). Samples were deposited onto zero background silicon sample holders and analyzed in the 2θ range between 20° and 80° with a step size of 0.04° and a collection time of 6 s. Identification of phases was made by comparison to the powder diffraction files (PDFs) of the International Center of Diffraction Data (ICDD) using Eva 5.1 software. The background was subtracted using EVA software for easier phase identification.

Rietveld analysis was carried out using the Bruker TOPAS version 6.0, using a pseudo-Voigt function model. Refinements of diffraction patterns were performed within space groups Fd-3 m:1, I4/m. The occupancies were set to nominal values and were not refined.

2.4. Scanning transmission electron microscopy (S(T)EM)

Scanning transmission electron microscopy (S(T)EM) was carried out on a Hitachi S-5500 FESEM (Krefeld, Germany) equipped with an INCA 350 energy-dispersion X-ray (EDS) analysis unit. Acceleration voltages of 30 kV and 20 kV were used for the images and the analyses, respectively. All samples were prepared by dropping a toluene suspension containing uniformly dispersed nanoparticles on a carbon film supported on a 300-mesh copper grid.

2.5. Transmission electron microscopy (TEM)

TEM bright-field, TEM high-angle annular dark-field imaging (HAADF), and TEM-EDS were performed using a spherical aberration-corrected field emission JEOL 2100F TEM operating at 200 kV. EDS mapping was performed using a JEOL Silicon Drift Detector.

2.6. Raman spectroscopy

Raman spectroscopy was carried out using a WITec alpha 300 R Confocal Raman device equipped with a 532 nm laser. Raman spectra were obtained after 20 accumulations for 20 s from 100 to 1250 cm^{-1}.

2.7. X-ray photoelectron spectroscopy

Spectra were collected on an Axis Ultra (Kratos Analytical) equipped with a Mg Kα X-ray source operating at 280 W Physical Electronics radiation source. The samples were analyzed under ultra-high-vacuum conditions (2.5×10^{-10} Torr base pressure). After recording a broad range spectrum (pass energy, 100 eV), high-resolution spectra were recorded for the C 1*s*, Ni 2*p*, Fe 2*p* and P 2*p* core XPS levels (pass energy, 200 eV). The binding energies were calibrated with respect to the C 1*s* peak at 284.8 eV. Spectrum processing was carried out using the Casa XPS software package.

2.8. Electrochemical characterization

Electrochemical characterization was carried out in a standard three-electrode rotating disc electrode (RDE) setup from Pine Instruments. Polished glassy carbon (GC) electrodes were used as working electrodes ($A = 0.196\ cm^2$, Pine Instruments) and a Pt mesh was used as a counter electrode. The working electrode potentials were measured versus a Hg|HgO reference electrode filled with 4.2 mol dm^{-3} KOH from Pine Instruments. Polytetrafluoroethylene (PTFE) containers were used both for electrochemical experiments and electrolyte preparation. All measurements were controlled using a Bio-Logic Potentiostat/Galvanostat (Model VMP3) in 1 mol dm^{-3} KOH (Fe-free electrolyte, 99.99 % and 85 % trace metal basis).

Cyclic and linear sweep voltammograms were collected at a rotation frequency of 1600 rpm. Polarization curves were collected using chronoamperometry with E_{appl} (applied potential) stepped from 1.4 to 1.7 V vs. RHE in 20 mV increments. At each potential step, steady-state data were collected at angular velocities (ω) corresponding to rotational frequencies of 2000 and 600 rpm. Data were also collected in the absence of disk rotation. Catalyst inks were prepared by dispersing 2.5 mg of the catalyst powders in a mixture of 750 μL of milli-Q water, 250 μL of 2-propanol, and 50 µL of Nafion (5 wt%). The inks were homogeneously dispersed by ultrasonication for 20 min and then 10 µL was drop-cast on the GC electrode to make up a final metal loading of 0.12 mg cm^{-2}. All electrochemical data were corrected for uncompensated series resistance after data collection. The uncompensated resistance of the cell was measured with a single-point high-frequency impedance measurement, and *IR* drop was compensated at 85 % through positive feedback using the Bio-Logic EC-Lab software. Our electrochemical cell typically had $R_u \sim 4\ \Omega$ in 1 mol dm^{-3} KOH. Electrochemical impedance spectroscopy measurements were carried out at five different overpotentials (0.6, 0.61, 0.615, 0.62, 0.625 V vs. Hg/HgO from 10 mHz to 1 MHz with an amplitude of 10 mV.

Prior to all catalytic tests, the electrode was first subjected to continuous potential cycling at 50 $mV^{-1}s$ in the potential range of 1.0 through 1.6 V vs.(RHE) until reproducible voltammograms were obtained.

The electrochemically active surface area (ECSA) was estimated from the double layer capacitance [53]. The double-layer capacitance, in turn, was estimated by cyclic voltammetry (CV) in a potential region in which faradaic currents can be assumed absent. The CV measurements

were conducted in a quiescent solution by sweeping the potential across this non-faradaic region from the more positive to negative potential and back at 7 different scan rates: 10, 30, 50, 70, 100, 200, and 300 $mV^{-1}s$. The working electrode was held at each potential vertex for 10 s before beginning the next sweep [54,55]. The double–layer capacitance was estimated from the slope of the plots of the charging current i_c vs. the scan rate ν as dictated by the equation

$$i_c = C_{dl} \times \nu \quad (1)$$

in which C_{dl} is the double-layer capacitance [55].

2.9. Estimation of the Faradaic efficiency using rotating ring-disk electrode

For rotating ring-disk electrode (RRDE) experiments, electrodes with various loadings (12–48 μg cm^{-2}) were employed. 500 μL of the ink described above was diluted with 500 μL of milli-Q water. An amount of the ink corresponding to the desired loading was drop-cast on to a working electrode. The working electrode was a RRDE with a GC disk (5 mm diameter) and a gold ring (7.5 mm outer diameter and 6.5 mm inner diameter) equipped with an MSR rotator system, both from Pine Research Instruments. The counter electrode was a smooth Pt wire and the reference electrode was a Hg/HgO electrode filled with 4.2 mol dm^{-3} KOH. All cyclic voltammograms (CVs) of the disk electrode were recorded at a sweep rate of 10 $mV^{-1}s$. The RRDE collection efficiency (24.1 % at 900 rpm) was determined from the ring and disk current ratios in 1 mol dm^{-3} KOH + 10 mol $dm^{-3}K_3[Fe(CN)_6]$ solution. The ring potential (+0.3 V vs. RHE) for RRDE studies of the OER was chosen based on previous reports for oxygen reduction reaction on a gold electrode [29,56]. Before each RRDE measurement, the gold surface of the ring electrode was cleaned by applying 100 potential cycles in the interval from 0.03 to 1.53 V at 100 mV s^{-1}.

2.10. Estimation of the Faradaic efficiency based on measuring the amount of generated O_2 gas

The Faradaic efficiency was also calculated using an eudiometer set-up (Figure S.10) based on collecting the generated oxygen gas bubbles by applying 10 mA (51 mA cm^{-2}) constant current. The amount of the generated O_2 was calculated from the volume of gas evolved corrected for the water vapour pressure and relating the amount of oxygen to the measured volume through the ideal gas equation. The theoretical amount of O_2 expected to be produced by applying 10 mA (51 mA cm^{-2}) was calculated from the electrical charge passed through the electrode using the Faraday equation:

$$n(\text{moles of produced } O_2) = \frac{It}{4F} \quad (2)$$

2.11. Calibration of Hg/HgO reference electrode and conversion to RHE

The calibration of the Hg/HgO electrode was performed in a standard three-electrode system with polished Pt foil as the working and counter electrodes, and the Hg/HgO electrode as the reference electrode. Electrolytes were pre-purged and saturated with 99.999 % H_2. Linear sweep voltammetry (LSV) was then performed at a scan rate of 0.5 mV s^{-1}, and the potential at which the current crossed zero was considered to be the thermodynamic potential for the hydrogen electrode reaction [57]. For example, in 1 mol dm^{-3} KOH, the zero current point appeared at − 0.900 V, and so the potential with respect to the reversible hydrogen electrode (RHE) is given by $E(\text{RHE}) = E(Hg/HgO) + 0.900$ V.

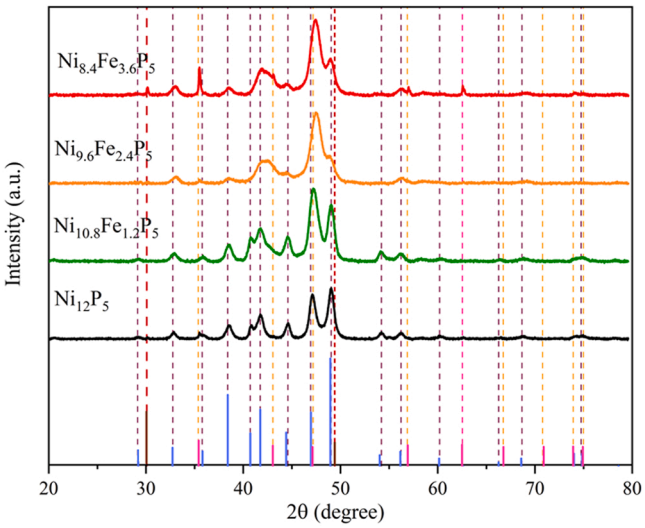

Fig. 1. XRD patterns for different targeted compositions of $Ni_{12-x}Fe_xP_5$ with $x = 1.2, 2.4, 3.6$. The light blue, pink, and brown dashed-drop lines indicate the reference pattern of $Ni_{12}P_5$, Fe_3O_4, and Fe_2O_3 phases respectively.

3. Results

3.1. Chemical and physical characterization

Fig. 1 shows the XRD patterns for the different target compositions. The XRD diffractogram for the nickel phosphide composition without any Fe unambiguously matches that of the pure $Ni_{12}P_5$-phase (tetragonal) structure (PDF 03-065-1623). For all iron-containing compositions, the diffraction peaks were shifted to larger angles compared to the corresponding peaks in the $Ni_{12}P_5$ diffractogram. As shown in Fig. 1, the $Ni_{10.8}Fe_{1.2}P_5$ nanoparticles crystallized in the same tetragonal phase as $Ni_{12}P_5$ nanoparticles, suggesting the formation of homogeneous Ni-Fe-P compositions with no detectable crystalline impurities.

However, clear changes in the diffractograms can be discerned upon further increase in the Fe content to above $x = 1.2$. At an Fe content to above $x = 1.2$, the peak at 49.2°, corresponding to the (312) plane of $Ni_{12}P_5$, dwindled while the intensity of the peak at 47.1°, corresponding to the (420) plane of $Ni_{12}P_5$, increased. Also, while the diffractogram for the composition with $x = 1.2$ contained the *same* peaks as the $Ni_{12}P_5$ catalyst, *new* peaks have emerged for the compositions with $x > 1.2$. This suggests the development of a second phase for $x = 2.4$, i.e. when the Fe content is increased beyond $x = 1.2$. This second phase is most likely an Fe_3O_4 phase; the new peaks at 35.16° and 31.7° agree well with the (101) and (211) planes of Fe_3O_4, respectively. The peak corresponding to the (420) plane in $Ni_{12}P_5$ overlaps with the peak corresponding to the (202) plane in Fe_3O_4. Therefore, the increase in the intensity at 47.1° with increasing Fe content can be attributed to a growing Fe_3O_4 phase. The peaks at 57° and 62.6° in $Ni_{8.4}Fe_{3.6}P_5$ belong to the (115) and (044) planes in Fe_3O_4. For $Ni_{8.4}Fe_{3.6}P_5$ ($x = 3.6$), Fe_2O_3 is formed as a third phase, and the reason for the higher intensity of the 49.2° peak than in NiFeP@Fe_3O_4($x = 2.4$) is likely to be due to its overlap with the (024) plane of Fe_2O_3. The emergence of the new peak at 32.7° is also attributed to the Fe_2O_3, viz. its (104) plane, which substantiates the suggested presence of an Fe_2O_3 phase.

Based on the Vegard's law for alloys, we would expect a linear relation between lattice parameters and the composition. However, such a linear behavior was not observed. This deviation from Vegard's law has been previously reported for $Fe_xNi_{2-x}P$ bulk solid solutions and nanoparticles, and has been attributed to an unequal distribution of the two different metals in sites of different size in the lattice [58,59].

The $Ni_{12}P_5$ tetragonal structure type has two metal coordination sites. The Ni atoms in the first site are surrounded by the four nearest P

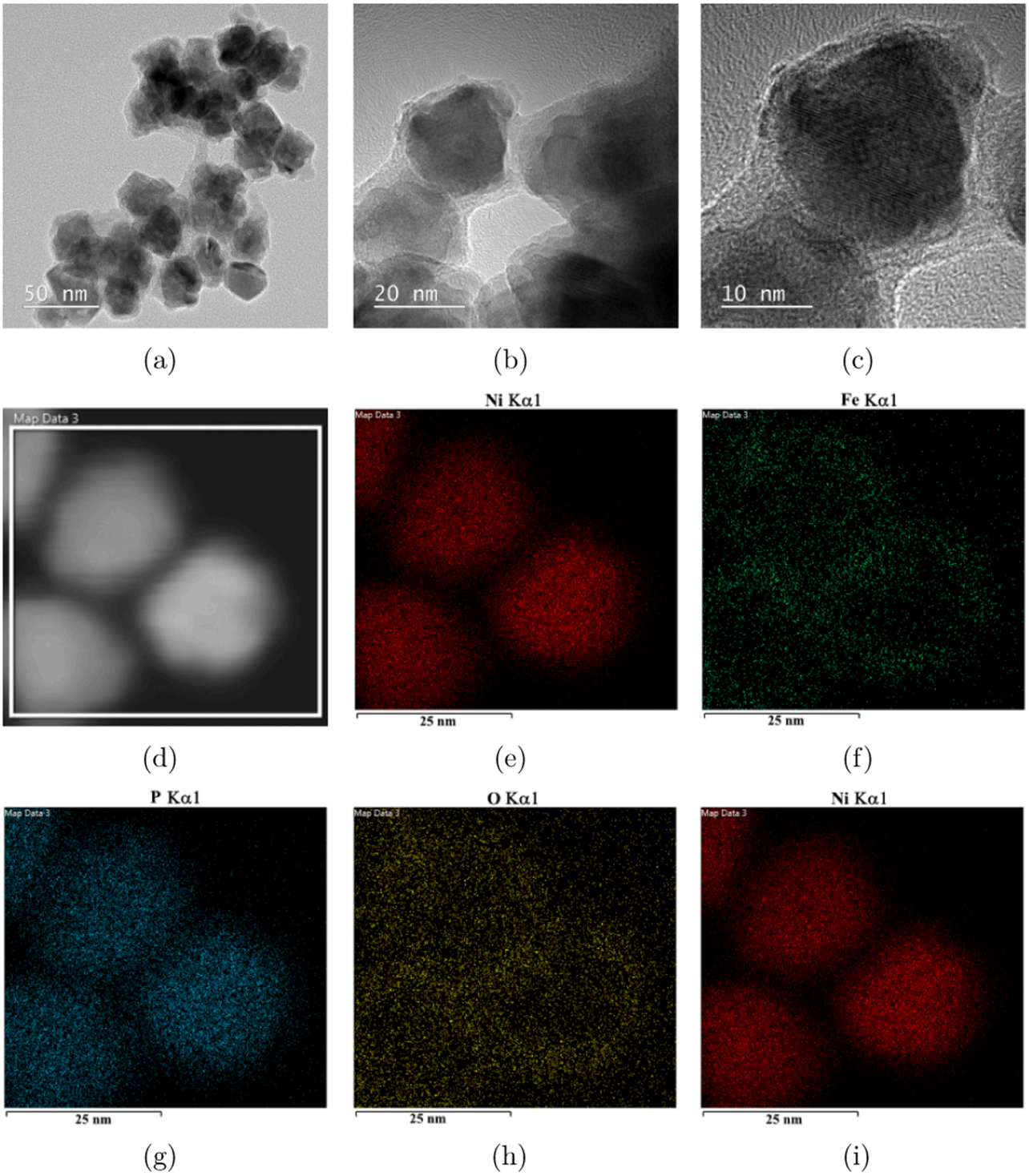

Fig. 2. (a) and (b) TEM images of as prepared NiFeP@Fe_3O_4($x = 2.4$) nanoparticles. (c) HR-TEM image of a single particle (d) HADAAF image of the selected area. (e)–(h) Single-element TEM-EDS maps describing the distribution of Ni, P, Fe, and O respectively. (i) Merged TEM-EDS elemental map.

atoms at distances 2.194–2.467 Å and eight Ni atoms located at 2.526–2.725 Å. There are 11 atoms forming coordination polyhedra around the second Ni site, viz. two nearest P atoms at 2.260 Å – 2.283 Å, five Ni atoms at 2.517–2.575 Å, two P atoms at 2.619 Å, and two Ni atoms at 2.725 Å [60]. The atomic radius of Fe is slightly larger than that of Ni 125 pm vs. 121 pm. Among the two available sites, we would normally expect Fe to occupy the larger one in $Ni_{12-x}Fe_xP_5$. This is the case for high Fe fractions. However, studies of bulk hexagonal structures, which also have two different metal sites, suggest that occupancy is dependent on composition; at low Fe metal fractions, the smaller site is preferentially occupied by Fe. Goodenough [61] has suggested that the preference of Ni for the larger site in Fe-poor compositions is due to electron transfer from Fe to Ni. X-ray photoelectron spectroscopy (XPS) and X-ray absorption near-edge spectroscopy (XANES) investigations of the $Fe_xNi_{2-x}P$ system [62] have revealed that the electron density of Ni atoms has been increased, presumably due to electron transfer from Fe to the more electronegative Ni atoms, consistent with this hypothesis.

Bright-field TEM images of $Ni_{12}P_5$ show that the catalyst consists of

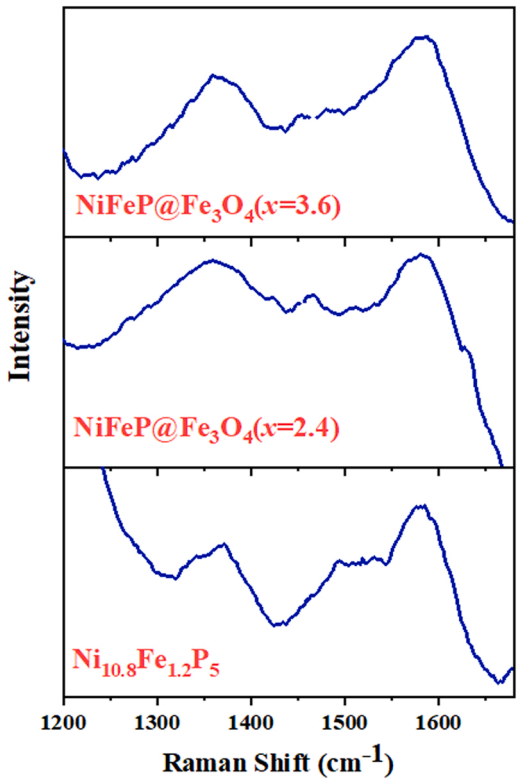

Fig. 3. comparison of bands at 1582c^{-1} and 1360 cm^{-1} in $Ni_{12-x}Fe_xP_5$ nanoparticles attributed to *D* and *G* band of carbon.

quasi-spherical nanoparticles with average diameter of 15.20 ± 2.25 nm. An example is given in Fig. S.1 in the Supporting Information. Analysis of the high-resolution TEM (HR-TEM) image (Fig. S.1(b)) gives lattice-fringe spacings of about 2.1 Å, corresponding to the (400) lattice plane of tetragonal $Ni_{12}P_5$. Energy-dispersive spectroscopy (EDS) in TEM indicate uniform distributions of Ni and P across the $Ni_{12}P_5$ nanoparticles (Fig. 1.2). Based on the EDS maps performed in the TEM, the apparent ratio of P:Ni was estimated to 0.38.

TEM images of $Ni_{12-x}Fe_xP_5$ nanoparticles (Fig. S.2, 2, and S.3) show that the quasi-spherical $Ni_{12}P_5$ nanoparticles were converted to highly faceted nanoparticles with pentagonal cross-sections in TEM upon addition of Fe. The size distribution became broader with increasing Fe content.

Analysis of the HR-TEM image of $Ni_{10.8}Fe_{1.2}P_5$ nanoparticles (Fig. S.2 (c)) revealed a D-spacing of 2.1 Å corresponding to the (400) plane of the $Ni_{12}P_5$ tetragonal crystal structure, which is consistent with the XRD results. Moreover, the EDS mapping confirmed the uniform distribution of Ni, Fe, P, and O across the particles. The EDS composition was in relatively good agreement with the targeted stoichiometry.

Upon increasing the Fe content to $x = 2.4$ and 3.6, the particles became more faceted and irregular in shape. Results of energy-dispersive spectroscopy (EDS) indicate a core-shell structure for the $Ni_{9.6}Fe_{2.4}P_5$ and $Ni_{8.4}Fe_{3.6}P_5$ nanoparticles (Fig. 2 and S.3) where Ni and P are evenly distributed in the core while Fe and O that reside in the shell dominate over that in the bulk. This partial segregation is compatible with the XRD patterns, which indicates the evolution of Fe_3O_4 as the second phase. The TEM images demonstrate that the Fe_3O_4 phase forms a shell surrounding a $Ni_{12-x}Fe_xP_5$ core, in which $1.2 < x$ (stoichiometry of Fe) < 3.6. The core is rich in Ni and P, while the shell is rich in Fe and O. For simplicity, we will refer below to these particles as NiFeP@Fe_3O_4($x = 2.4$) for the sample of nominal composition $x = 2.4$ or NiFeP@Fe_3O_4($x = 3.6$) for the sample of nominal composition $x = 3.6$, while referring to the compositions in the general sense as $Ni_{12-x}Fe_xP_5$ as before when the catalyst architecture is not important.

Table 2
D-band and G-band positions of carbon layer in $Ni_{12-x}Fe_xP_5$ nanoparticles.

Composition	D-band (cm^{-1})	G-band (cm^{-1})	I_D/I_G
NiFeP@Fe_3O_4($x = 3.6$)	1359	1580	0.96
NiFeP@Fe_3O_4($x = 2.4$)	1354	1578	0.98
$Ni_{10.8}Fe_{1.2}P_5$	1367	1576	0.94

Close inspection of the TEM images of $Ni_{12-x}Fe_xP_5$ nanoparticles reveals the existence of a relatively regular coating at least partly covering the NiFeP@Fe_3O_4 particles (Fig. 2(b) and (c)). The thickness of this layer varies from catalyst to catalyst and it is more developed (thicker) for NiFeP@Fe_3O_4($x = 2.4$), and NiFeP@Fe_3O_4($x = 3.6$) in comparison with $Ni_{10.8}Fe_{1.2}P_5$.

Raman spectra of the synthesized $Ni_{12-x}Fe_xP_5$ nanoparticles are shown in Fig. 3. The peak positions are listed in Table 1. All the recorded spectra were subjected to a Voight-based deconvolution analysis.

The data in Table 1 show that when the Fe content increases all peaks below 350 cm^{-1} are blue-shifted and those with wavenumbers higher than 1105 cm^{-1} are red-shifted. As indicated in Fig. S.4 some of the observed peaks were attributed to NiO and FeO_x species [63,64]. In all Raman spectra of $Ni_{12-x}Fe_xP_5$ nanoparticles, Fig. 3, two peaks at around 1582 and 1360 cm^{-1} can be clearly seen. For comparison, similar peaks were also observed at the glassy-carbon electrode used for the electrochemical measurements, see Section 3.3 below Table 2.

XPS survey spectra recorded for $Ni_{12-x}Fe_xP_5$ (see Figure S.5 in the Supporting Information) show clear peaks corresponding to Fe which are not present in the spectrum for the pure $Ni_{12}P_5$ phase. This indicates the successful incorporation of Fe in the former samples.

Fig. 4 (a) shows the Ni 2*p* XPS core-level spectra of the synthesized nanoparticles. The Ni 2*p* spectrum contains two main peaks, resulting from the spin-orbit splitting of the p orbital that are assigned as Ni $2p_{3/2}$ (850–865 eV) and Ni $2p_{1/2}$ (865–885 eV). The Ni $2p_{3/2}$ region was further deconvoluted into three peaks for $Ni_{12}P_5$, NiFeP@Fe_3O_4($x = 2.4$), and NiFeP@Fe_3O_4($x = 3.64$). However, since the satellite and oxidized Ni was quite well-separated for $Ni_{10.8}Fe_{1.2}P$, the Ni $2p_{3/2}$ region was therefore deconvoluted into four peaks. The peak at 853 eV can be related to both Ni and Ni-P [13]. Unfortunately, an unambiguous separation of the contributions from these two species through XPS is challenging. A previous study by Li *et al.* attributed both Ni and Ni-P to the same *BE* of 853.1 eV, [65] while others have tabulated Ni(0) at 852.7 eV and Ni_2P at 852.9 eV, only 0.2 eV apart [66]. We therefore made no attempt at separating the two contributions here. However, for NiFeP@Fe_3O_4($x = 3.6$) the peak at 854.4 eV can be exclusively assigned to Ni-P [67].

Regarding the shift in Ni 2*p* peaks with addition of Fe, there is evidence in the literature [61,62] showing that electron transfer from Fe to Ni will take place in nickel iron phosphide compounds, which in turn increases the electron density of Ni atoms. Considering the fact that Ni atoms have higher electron density upon addition of Fe, we would

Table 1
Raman Bands of $Ni_{12-x}Fe_xP_5$ nanoparticles.

Composition	Raman Peak Position (cm^{-1})									
NiFeP@Fe_3O_4($x = 3.6$)	189	244	313	356	447	475	556	623	667	1082
NiFeP@Fe_3O_4($x = 2.4$)	190	267	322	376	–	486	565	–	664	1095
$Ni_{10.8}Fe_{1.2}P_5$	201	270	328	378	–	–	566	–	670	1097

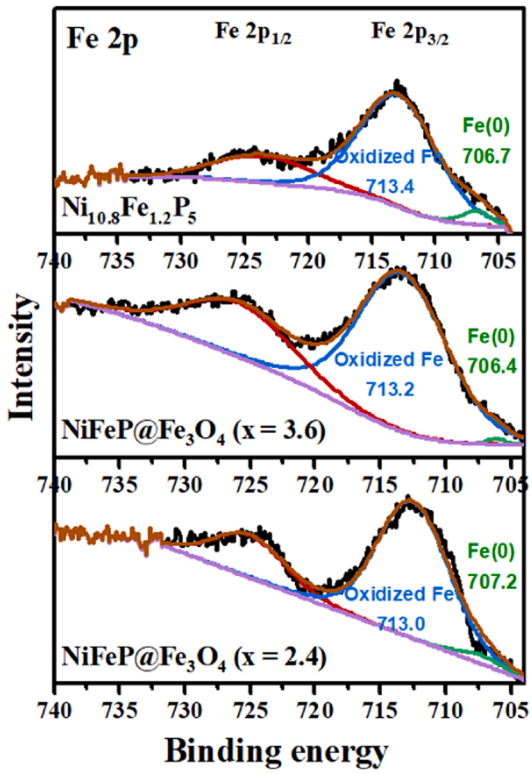

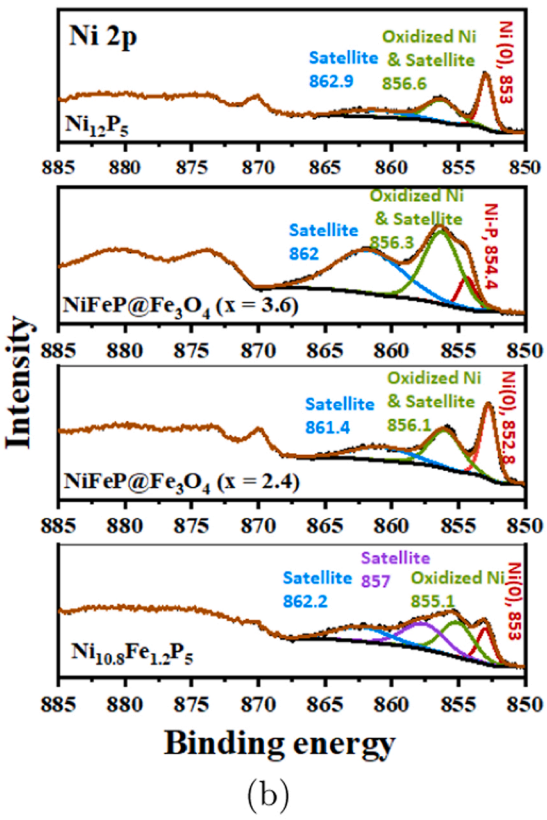

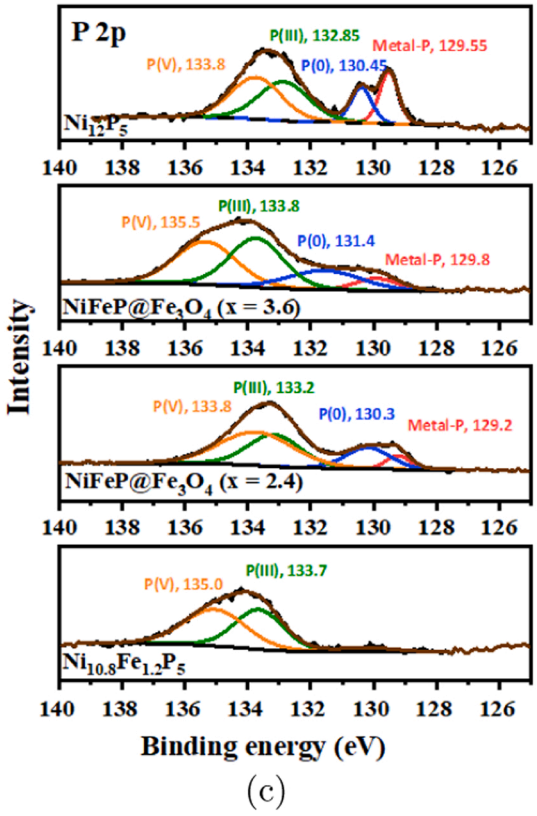

Fig. 4. Regional scans of as-prepared $Ni_{12-x}Fe_xP_5$ nanoparticles. (a) Ni 2p region. (b) P2p region. (c) Fe 2p region.

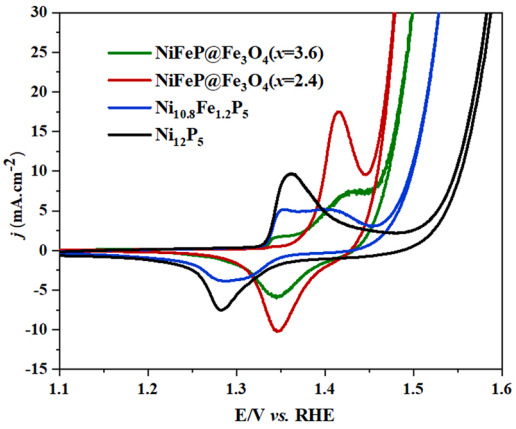

Fig. 5. Cyclic voltammograms of $Ni_{12-x}Fe_xP_5$ catalysts for $x = 0$, 1.2, 2.4, 3.6.

expect a shift to lower binding energies in Ni. This is in accordance with our experimental results.

The XPS spectra for the as-synthesized $Ni_{12-x}Fe_xP_5$ nanoparticles (Fig. 4) could be fitted to an Fe $2p_{3/2}$ peak at 712.15 eV and an Fe $2p_{1/2}$ peak at 724.18 eV. This indicates that two distinct Fe species are present in the samples. The Fe $2p_{3/2}$ peak can, in turn, be decomposed into two peaks approximately at 706 and 713 eV, respectively originating from the iron(0) and oxidized iron [68].

For all the catalysts except $Ni_{10.8}Fe_{1.2}P_5$, the P 2*p* region was deconvoluted into four peaks. For the $Ni_{12}P_5$ catalyst, components at 129.4, 130.4, 132.6 and 133.3 eV, corresponding to phosphide, P(0), P (III) and P(V) species, respectively [69,70], proved to fit the spectra well. The values were in good agreement with the corresponding values reported for $Ni_{12}P_5$ in the literature [71]. The P(V) and P(III) components have been interpreted as surface phosphate and phosphite [70], respectively. These may have formed as a result of the exposure of the nanoparticles to air while being stored at the ambient conditions. Upon addition of Fe, a noticeable shift is observed in all the components, possibly due to the interaction of P with Fe. It is also worth noting that the fraction of oxidized phosphorous is larger in Fe-containing nanoparticles than in $Ni_{12}P_5$, which indicates that the addition of Fe makes particles more vulnerable to oxidation. The ratio of oxidized to non-oxidized phosphorous species increases in the order of $Ni_{10.8}Fe_{1.2}P_5$ > NiFeP@Fe_3O_4($x = 3.6$) > NiFeP@Fe_3O_4($x = 2.4$), which is opposite of the order in terms of the thickness of the self-generated carbon layer. Therefore, it is reasonable to conclude that the carbon layer to some extent protects the particles from oxidation. For the $Ni_{10.8}Fe_{1.2}P_5$ nanoparticles with the thinnest carbon layer, the metal-P (phosphide) and P(0) species were barely detectable, indicating negligible carbon-layer protection and extensive surface oxidation of nanoparticles. All the parameters obtained from fits to the XPS data are presented in Table S.1.

3.2. Electrochemical characterization

Fig. 5 shows cyclic voltammograms of $Ni_{12-x}Fe_xP_5$ catalysts. For comparison, an Fe-free $Ni_{12}P_5$ catalyst was also tested as a benchmark compound to explore the effect of the addition of Fe on the electrocatalytic activity. The CVs for all the tested catalysts contained redox peaks at potentials below the onset of the oxygen evolution reaction, attributed to Ni^{3+}/Ni^{2+}. However, the peak position differs depending on the composition of the catalyst.

For the $Ni_{12}P_5$, the anodic redox peak appears at $E_{anodic} = 1.36$ V in the CV and the cathodic peak at $E_{cathodic} = 1.28$ V. Interestingly, upon addition of Fe the anodic redox peak is shifted towards positive potentials. The anodic peak in $Ni_{10.8}Fe_{1.2}P_5$ is split into two peaks (~ 1.34 and 1.40 V) whereas the cathodic peak is observed at the same potential as $Ni_{12}P_5$.

Splitting of the anodic peak is also observed for the NiFeP@Fe_3O_4($x = 3.6$) catalyst. A wider separation of the peaks was observed in this case, however, with peak positions at $E_{anodic} = 1.34$ and 1.42 V. The splitting of the anodic peak suggests two types of Ni sites in the particles, one corresponding to Ni sites in $Ni_{12}P_5$ and another at which Ni interacts with Fe. The absence of any cathodic split maybe related to sluggish kinetics. The cathodic peak shifts to the more positive potential of 1.34 V. Finally, the cyclic voltammogram of the NiFeP@Fe_3O_4($x = 2.4$) catalyst shows a redox peak without any splitting at $E_{anodic} = 1.41$ V and $E_{cathodic} = 1.34$ V.

The shift in the Ni^{3+}/Ni^{2+} redox peak to more positive potentials upon addition of Fe is well documented, and has generally been attributed to the stabilization of the Ni^{2+} state in the presence of Fe [72–74]. The larger peak current in the case of NiFeP@Fe_3O_4($x = 2.4$) is opposite of what is normally reported in the literature [75,76], and the effect of Fe is usually that of reducing the peak current density.

Fig. 6 shows the linear sweep voltammograms for the $Ni_{12-x}Fe_xP_5$ catalysts. Fig. 6 also includes polarization curves recorded by chronoamperometry, which are in excellent agreement with those recorded by linear sweep voltammetry. The overpotential needed for all tested catalysts to deliver 10 and 50 mA cm^{-2} (i.e. η_{10} and η_{50}) are tabulated in Table 3. To reach the benchmark current density η_{10} at the $Ni_{12}P_5$, an overpotential of 301 mV is needed, while NiFeP@Fe_3O_4($x = 2.4$) merely requires an overpotential of 220 mV, showing a significant improvement in the OER activity. The apparent OER activity per mass for all the tested catalysts follows the order: $Ni_{12}P_5$ < $Ni_{10.8}Fe_{1.2}P_5$ < NiFeP@Fe_3O_4($x = 3.6$) < NiFeP@Fe_3O_4($x = 2.4$).

The polarization curves presented in Fig. 6 all show an up-turn at high overpotentials, which is a common feature of plots of electrode potential vs. the logarithm of current for the OER as presented in the literature [77–80,81,82]. Such changes in the slope $dE/d\log i$ with increasing potential are most often attributed to either a change in the rate-determining step (*rds*) within a given pathway [79] or to saturation or depletion of intermediates at the surface [77]. The degree of consistency between the data recorded by LSV and CA, suggests that the dual-slope behavior is mechanistically significant and not due to electrode blocking, mass-transport limitations or ohmic effects. Kinetic parameters, including Tafel slopes (i.e. $dE/d\log i$), determined from the lower overpotential region (below the up-turn) are presented in Table 3.

The results of EIS measurements, plotted as Tafel impedance (Z_t), at different overpotentials for $Ni_{12-x}Fe_xP_5$ with ($x = 0$, 1.2, 2.4, 3.6) are shown in Fig. 7. Z_t was computed from the impedance by multiplication of the latter with the steady-state current density as [83],

$$Z_t = \frac{\widetilde{E}}{\widetilde{i}} i_{ss} \tag{3}$$

where $\widetilde{E}$ is the potential amplitude, $\widetilde{i}$ the current-density amplitude, and i_{ss} is the steady-state current density. (The ohmic resistance, as assessed from the high-frequency intercept of the impedance-plane plot with the real axis, was subtracted from all data prior to the conversion to Tafel impedance). As can be seen, the low-frequency intercept increases slightly as the overpotential is increasing. In these plots, the dE/dlogi slope can be read off as the value of the low-frequency intercept with the real axis [84,85]. For all samples the diameter of the arc in the Tafel-impedance plane plot are in reasonable agreement with the slopes from the steady-state curves, Fig. 6. However, due to some ambiguity in determining the appropriate region to use for fitting the steady-state data, we consider the Tafel slopes obtained through impedance to represent the more accurate of the two sets of values. The Tafel slopes from the impedance data cluster around 40 mV for all the iron-containing samples ($Ni_{10.8}Fe_{1.2}P_5$, NiFeP@Fe_3O_4, and NiFeP@-Fe_3O_4), whereas the Tafel slope for $Ni_{12}P_5$ is significantly higher, 60 mV).

Data from which the double-layer capacitances (C_{dl}) were evaluated and the ECSA were estimated, are given in the Supporting Information

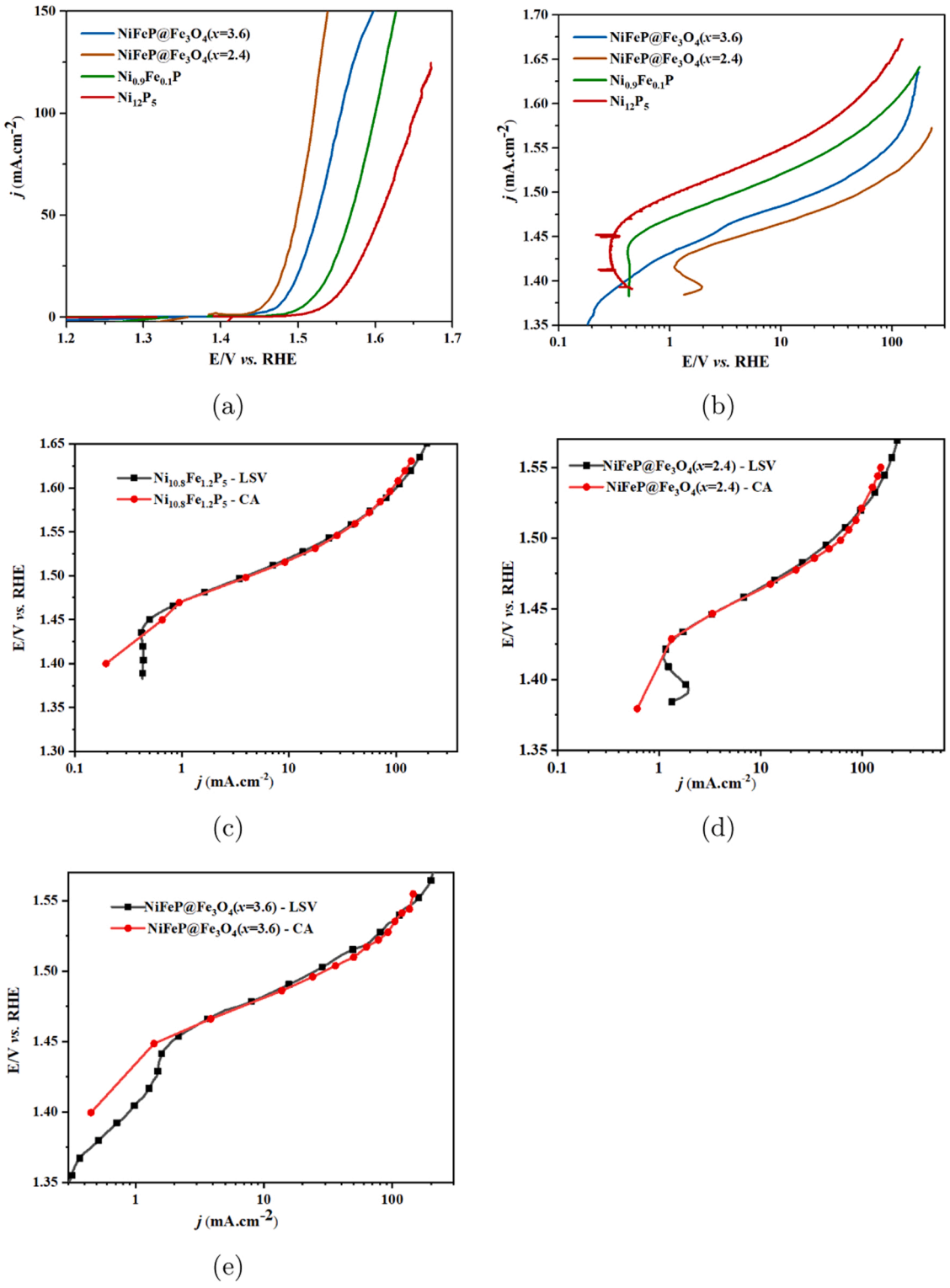

Fig. 6. (a) and (b) Comparison of the linear sweep voltammograms and polarization plots of $Ni_{12-x}Fe_xP_5$ catalysts in 1 mol dm^{-3} KOH. (c), (d), and (e) Polarization plots acquired from linear sweep voltammetry and chronoamperometry techniques for $Ni_{10.8}Fe_{1.2}P_5$, NiFeP@Fe_3O_4($x = 2.4$), and NiFeP@Fe_3O_4($x = 3.6$) respectively. The close overlay of the data suggests good approximation of steady-state conditions.

(Fig. S.6). C_{dl} values of 3.35, 3.56, 2.85 and 2.26 mF cm^{-2} were obtained for NiFeP@Fe_3O_4($x = 2.4$), NiFeP@Fe_3O_4($x = 3.6$), $Ni_{10.8}Fe_{1.2}P_5$, $Ni_{12}P_5$ respectively. In general, the double layer capacitances and hence the ECSA for the iron-containing $Ni_{12-x}Fe_xP_5$ catalysts were found to be larger than those for the $Ni_{12}P_5$ catalyst. In effect, the C_{dl} value is increasing along with the thickness of the carbon shell.

Fig. 8 compares the mass activity and overpotential of the NiFeP@Fe_3O_4($x = 2.4$) catalyst in this work with data for other catalysts based on non-precious metals as collected by Kibsgaard and Chorkendorff [86]. As can be seen from the plot, the NiFeP@Fe_3O_4($x = 2.4$) catalyst is among the best catalysts reported so far, displaying a mass activity of 0.1 A mg^{-1} and an overpotential of 220 mV at 10 mA cm^2_{geo}.

Table 3
Kinetic parameters for $Ni_{12-x}Fe_xP_5$ catalysts.

Catalyst	η_{10} (m V)	η_{50} (m V)	b (m Vdec^{-1})	b (Impedance) (m Vdec^{-1})
$Ni_{12}P_5$	301	380	65	60
$Ni_{10.8}Fe_{1.2}P_5$	290	330	39	45
NiFeP@Fe_3O_4($x = 2.4$)	220	270	40	37
NiFeP@Fe_3O_4($x = 3.6$)	250	290	50	45

Faradaic efficiencies of ~ 95 % and ~ 97 % (see the Supporting Information) were estimated from measurements of the volume of the collected gas and by use of a ring-disc electrode (see Section 2.9).

3.3. Stability and post-mortem characterization

In addition to the high OER catalytic activity, the NiFeP@Fe_3O_4($x = 2.4$) catalyst also showed a high stability under OER conditions, as measured by 500 potential cycles between 1.1 and 1.7 V at a scan rate of 10 mVs^{-1} (Fig. 9(a)). From cycle 10 to cycle 500 the current at 1.525 V decreased from 140 mA cm^{-2} to 100 mA cm^{-2}. There is no noticeable decrease in the charge associated with the anodic redox peak at 1.43 V and the corresponding cathodic peak at 1.35 V. There is, however, a slight shift to lower potentials with increasing number of scans. It is well-known that the addition of Fe to Ni catalysts will shift the redox peak to higher potentials. Therefore, we associate the shift in the peaks to lower overpotentials to a slight change in the surface composition and a concomitant change (8 %) in the catalytic activity also visible in the figure. The chronoamperometric measurement involved applying a constant current of 50 $mAcm^{-2}$) for 10 h (Fig. 9(b)) in 1 mol dm^{-3}. No noticeable increase in the potential was observed after 10 h, indicating that NiFeP@Fe_3O_4($x = 2.4$) is very stable.

Fig. 10 and Fig. S.7 exhibit TEM images of the semi-spherical NiFeP@Fe_3O_4($x = 2.4$) nanoparticles and the corresponding EDS mappings after they had been subjected to a constant 10 mA current for 5 h. The TEM-EDS mapping of NiFeP@Fe_3O_4($x = 2.4$) nanoparticles (Fig. S.7) shows that phosphorus remains a part of the catalyst after exposure to the OER conditions. The bulk Ni:P ratio was 2.5, essentially similar to that of the as-prepared nanoparticles, with the Ni:P ratio of 2.7 prior to the test.

Fig. 10(b) shows the HR-TEM images of two adjacent NiFeP@Fe_3O_4($x = 2.4$) nanoparticles. The images are similar to those in Fig. 2(b) and (c), and the coating covering the particles that is visible in Fig. 2(b) and (c) is still intact after exposure to the electrolyte and high electrode potentials associated with the OER. The HR-TEM image of the particles also shows crystalline domains at their center, but somewhat less crystalline domains at their periphery.

Fig. 3 shows the Raman spectra of as-prepared NiFeP@Fe_3O_4($x = 2.4$)/GC (glassy carbon) electrodes and the same sample after immersion for 10 min, and after the sample had been subjected to 100 cycles between 1 and 1.7 V and a constant current of 10 mA (50 mA cm^{-2}) for 2 h. A large peak at 1100 cm^{-1} in the NiFeP@Fe_3O_4($x = 2.4$) powder in the Raman spectra prior to mixing the

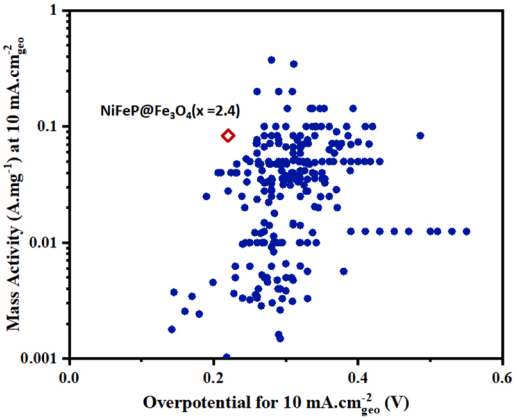

Fig. 8. Comparison of mass activity and overpotential of non-precious-metal-based catalysts for oxygen evolution reaction in 1 mol dm^{-3} alkaline solution. Blue dots present the data reported in literature. Data were plotted based on the table was presented in Ref. [86]. The red diamond (◇) is the mass activity of the NiFeP@Fe_3O_4($x = 2.4$) catalyst presented in current work.

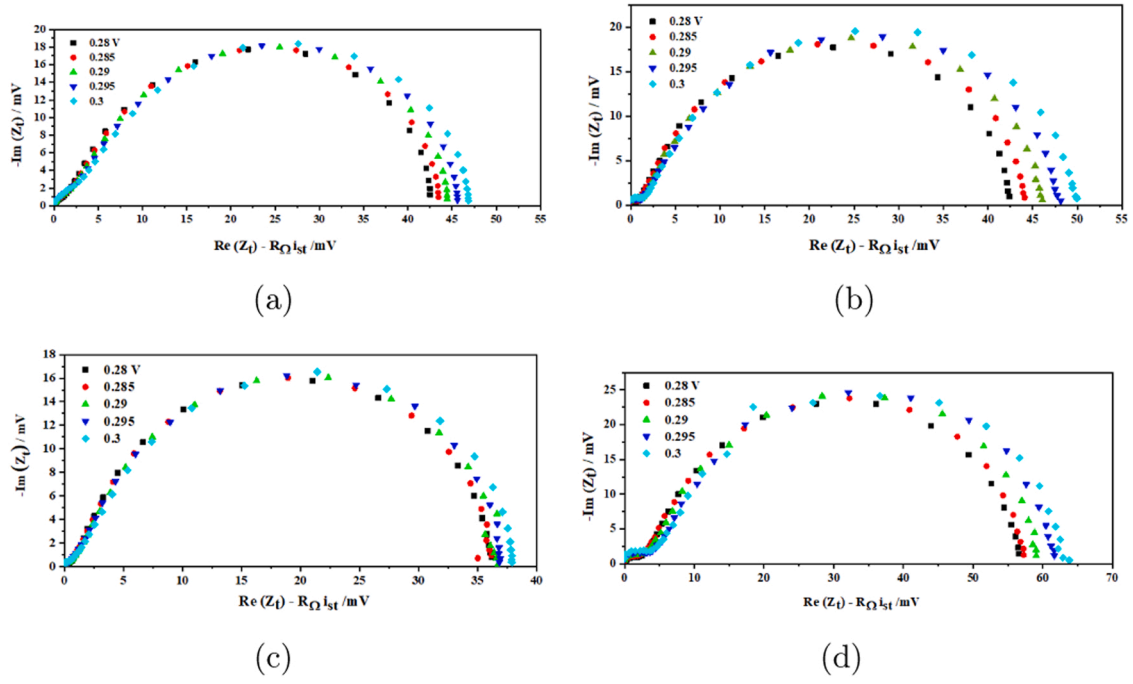

Fig. 7. Impedance-plane plot of Tafel impedance of (a) NiFeP@Fe_3O_4($x = 3.6$), (b) $Ni_{10.8}Fe_{1.2}P_5$, (c) NiFeP@Fe_3O_4($x = 2.4$), and (d) $Ni_{12}P_5$. The high frequency resistance (intercept) has been subtracted from all real values in the plots.

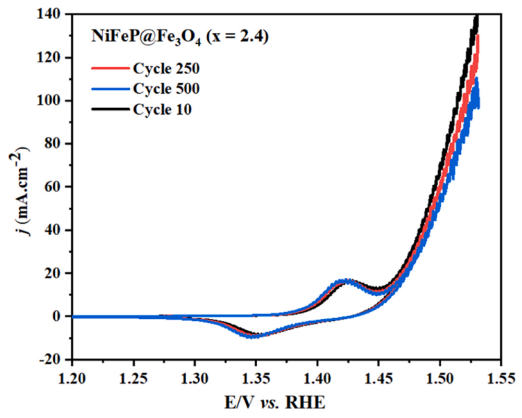

(a)

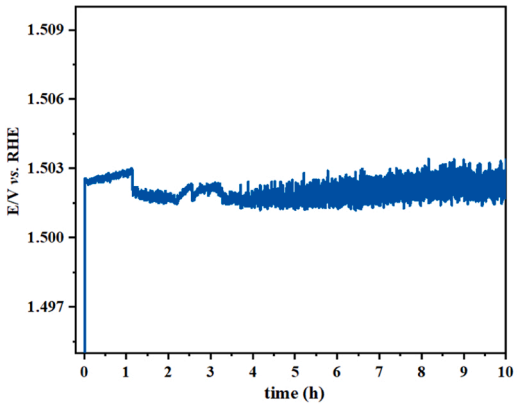

(b)

Fig. 9. (a) Cyclic voltammograms of NiFeP@Fe_3O_4($x = 2.4$) after 10, 250, and 500 cycles at a scan rate of 10 mVs^{-1} in 1 mol dm^{-3} KOH. (b) Time dependence of the potential at constant current density of 50 mA in 1 mol dm^{-3} KOH for 10 h.

ink (Fig. 3) is no longer present in the spectra of the same catalyst on the GC electrode, i.e. post mortem (Fig. 3). We associate this with dissolution of phosphate/phosphite species during the ink preparation. Apart from that, no other change was observed related to the changing/reorganization of the NiFeP@Fe_3O_4($x = 2.4$) catalyst after OER.

4. Discussion

Apart from their high mass activity and current efficiency for the OER, the most prominent feature of the $Ni_{12-x}Fe_xP_5$ catalysts is the presence of a coating both in the pristine catalysts as in Fig. 10(b), and post mortem as in Fig. 2(b) and (c). Regarding the fact that nanoparticles were synthesized in the presence of organic compounds (i.e. oleylamine and TOP), it is likely that the layer consists of carbon which has been generated upon decomposition of organic moieties adhered on the nanoparticles during the synthesis [69]. However, according to Jung et al. [51] and considering the fact that carbon atoms can be absorbed inside the lattice of the metal nanoparticles where metal acetylacetonate is used as a metal precursor [87], another possibility for the formation of the carbon layer could be the diffusion of carbon atoms from the interior of the metal nanoparticles to their surfaces in the phosphidation step at 300 °C. Moreover, the fact that the layer is invisible in the high-angle annular dark-field image of NiFeP@Fe_3O_4($x = 2.4$) (Fig. 2(d)) is consistent with the layer being composed of a lighter element, such as carbon, than those of the catalyst particle itself.

The bands peaking at wavenumbers 1582c^{-1} and 1360 cm^{-1} in Fig. 3 are consistent with the G- and D-bands, respectively, for carbon samples [88], and supports the suggestion that a carbon layer has been formed at the particle surfaces. The G-band is associated with an ordered graphite structure and the D-band with defects, respectively. The peak height ratios I_D:I_G are 0.98 for NiFeP@Fe_3O_4($x = 2.4$) (Fig. 3), 0.96 for NiFeP@Fe_3O_4($x = 3.6$), and 0.95 for the $Ni_{10.8}Fe_{1.2}P_5$. The higher ratio found for NiFeP@Fe_3O_4($x = 2.4$) indicate a more defective nature and porous structure of the carbon layer [88] for this sample.

The fact that the particle size is quite narrow, Fig. S5, makes it likely that at least the majority of the particles have been coated by carbon. A narrow particle size distribution indicates that the oleylamine and TOP were efficient in preventing particle growth, and therefore organic residues will coat all particles within the dominating size range. It is these residues that would be converted to carbon in the heating step, hence coating all particles within the size range indicated in Fig. S5.

We therefore conclude that the coating covering the catalyst particles is a self-generated layer of carbon coming from ligand decomposition, with some possible doping by nitrogen or phosphorus from the ligands or even Fe [89] or Ni from the metal precursor. This layer only forms with iron present in the nanoparticles. Therefore, it is probably catalyzed by iron and therefore only present in the bimetallic system. The process of formation is therefore somewhat analogous to that suggested for the growth of carbon nanotubes on NiP amorphous nanoparticles, in the absence of any Fe, by annealing at the substantially higher temperature of 400 °C in an inert atmosphere [69,90].

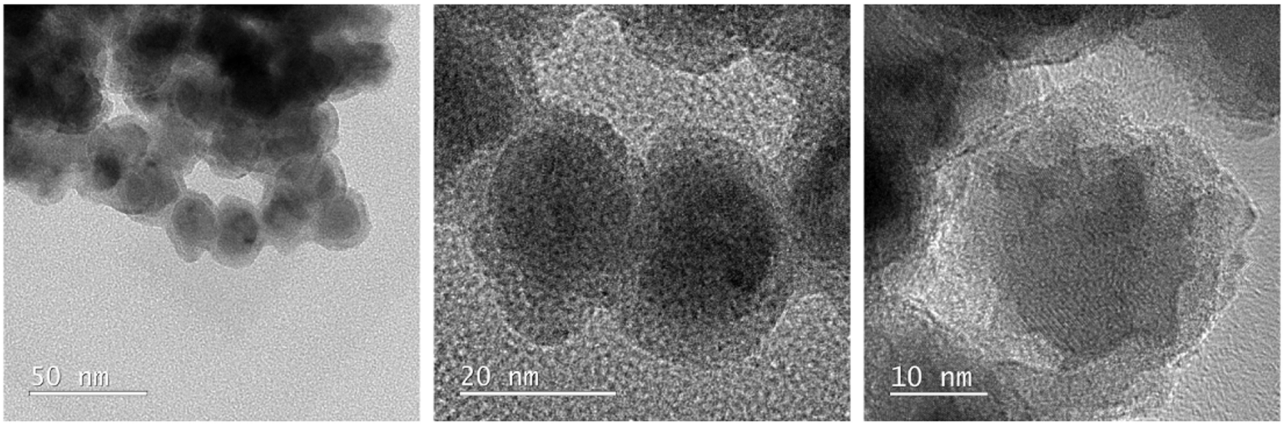

Fig. 10. Post-mortem TEM images of NiFeP@Fe_3O_4($x = 2.4$) catalysts after applying a constant current at 50 mA cm^{-2} for 5 h in 1 mol dm^{-3} KOH.

The differences in the ECSA (and in the peak heights in the voltammograms in Fig. 5 between the different catalysts are a likely manifestation of the carbon coating. This is because a carbon layer may help keeping catalyst particles apart and prevent agglomeration. As has been reported previously, one of the main advantages of carbon encapsulation of nanoparticles is the increase of the active surface area as a consequence of reduction in the agglomeration of nanoparticles [33, 91,92]. The NiFeP@Fe_3O_4($x = 2.4$) catalyst showed the highest C_{dl} and also has the thickest self-generated carbon layer, whereas the $Ni_{12}P_5$ nanoparticles showed the lowest C_{dl} among all tested catalysts and which have negligible carbon coverage. Presumably, carbon layers separate particles from each other and provide more area due to an increased access to some "inner surfaces" and leads to higher C_{dl}. These observations suggest that the presence and thickness of the carbon coverage display a prominent role in the obtained value for C_{dl} and consequently in the electrochemical active surface area.

Oxygen evolution at catalysts covered by a carbon layer would require transport of reaction products and reactants either directly through the layer itself or through pinholes in the layer. Reaction through pinholes is not likely due to the very high activity of these catalysts; the catalytic activity would have to be rather extreme to explain this, and this is not compatible with the stability measurements indicating that the carbon layer does protect the catalysts. According to the Pourbaix diagrams, most transition metal phosphides will not be stable under OER conditions [32]. The fact that our catalysts are stable, indicates that the layer does keep the phosphides from disintegrating.) A direct influence of the metal on the carbon as suggested by Cui et al. for carbon monolayers [34] is not likely in view of the thickness of the carbon layers in this work. Also, the observation of pronounced pre-catalytic redox peaks attributed to Ni^{3+}/Ni^{2+} (Fig. 5) rules out carbon as being the only electrochemically active site. Other options are diffusion of iron into the carbon creating a carbon iron catalyst [89] or exfoliation of the carbon layer, providing electrolyte access to the metal sites underneath [45]. However, our post-mortem TEM images clearly shows that the carbon layer is completely preserved after being exposed to the OER conditions, excluding exfoliation of the carbon layer as a possibility.

The quite intense Ni^{3+}/Ni^{2+} redox peak shows that the surface of the $Ni_{12-x}Fe_xP_5$ particles caged inside the carbon layer is electrochemically active. Therefore, this $Ni_{12-x}Fe_xP_5$ surface is likely to contribute significantly to the catalytic activity in the OER potential region as well. We tentatively propose a mechanism in which the hydroxide anions are transported through the carbon layer, possibly in a fashion similar to intercalation. Slow reaction steps are catalyzed at the $Ni_{12-x}Fe_xP_5$ surface, and reaction intermediates formed in steps downstream of the rate-determining step are transported by diffusion in the graphitic or disordered carbon layers, again in a similar fashion to intercalation. The exact details of theses processes will, however, have to await further investigation beyond the scope here.

5. Conclusion

A solution phase synthetic method for discrete $Ni_{12-x}Fe_xP_5$ ($x = 0$, 1.2, 2.4, 3.6) nanoparticles was developed. The ternary $Ni_{10.8}Fe_{1.2}P_5$ nanoparticles have a tetragonal crystal structure corresponding to that of $Ni_{12}P_5$, indicating the formation of a uniform Ni-Fe-P alloy. However, the XRD results showed that for the $x > 1.2$, particles with a core-shell structure were formed, in which a NiFeP alloy forms the core and Fe_3O_4 the shell (NiFeP@Fe_3O_4). A detailed inspection of the TEM images revealed that in effect a self-generated porous carbon layer covers $Ni_{12-x}Fe_xP_5$ nanoparticles. This carbon layer is formed as a result of the decomposition of organic precursors during synthesis. We observed no such carbon layer for $Ni_{12}P_5$ nanoparticles synthesized under the same conditions, i.e with $Ni_{12}P_5$ catalysts not containing iron. This suggests that the decomposition of organic compounds are catalyzed by the bimetallic system (i.e. NiFe). Encapsulation of the particles with carbon was further substantiated with Raman spectroscopy, in which the two characteristic peaks of carbon at 1395 and 1520 cm^{-1} were clearly observed and are attributed to the carbon D and G-band, respectively. Based on the TEM images, the self-generated porous carbon layer was thickest (~ 5 nm) for NiFeP@Fe_3O_4($x = 2.4$) nanoparticles and thinnest (~ 1 nm) for $Ni_{10.8}Fe_{1.2}P_5$ nanoparticles. All the as-synthesized nanoparticles were applied as electrocatalysts for the OER. The activity for the OER increases in the order $Ni_{12}P_5$ < $Ni_{10.8}Fe_{1.2}P_5$ < NiFeP@Fe_3O_4($x = 3.6$) < NiFeP@Fe_3O_4($x = 2.4$). NiFeP@Fe_3O_4 ($x = 2.4$) nanoparticles showed an extraordinary electrocatalytic activity by achieving 10 mA cm^{-2} at 220 mV. A difference in the Tafel slopes between catalysts containing iron and $Ni_{12}P_5$ indicates that the reaction mechanism for the OER changes as iron is included in the composition. Post-mortem TEM characterization of NiFeP@Fe_3O_4($x = 2.4$) showed that the carbon layer is very stable and is preserved after OER, consistent with in-situ Raman spectra which did not show any significant structural change upon exposure to the potentials at which the OER proceeds (1.6 V/51 mA cm^{-2}) for 5 h.

Declaration of Competing Interest

The authors declare that they have no known competing financial interests or personal relationships that could have appeared to influence the work reported in this paper.

Acknowledgements

The authors acknowledge the financial support from the Norwegian University of Science and Technology (NTNU) (project no. 81771154).

CRediT authorship contribution statement

Fatemeh Poureshghi: Conceptualization, Investigation, Methodology, Writing – original draft, Writing – review & editing. **Frode Seland:** Supervision, review, Methodology. **Jens Oluf Jensen:** Funding acquisition, Supervision, review, Methodology. **Svein Sunde:** Funding acquisition, Conceptualization, Supervision (investigation), Methodology, Writing – review & editing, Project administration.

Appendix A. Supporting information

Supplementary data associated with this article can be found in the online version at doi:10.1016/j.apcata.2022.118786.

References

[1] D. Pletcher, X. Li, Int. J. Hydrog. Energy 36 (23) (2011) 15089–15104, https://doi.org/10.1016/j.ijhydene.2011.08.080. ⟨http://www.sciencedirect.com/science/article/pii/S0360319911020015⟩.
[2] D. Xu, M.B. Stevens, M.R. Cosby, S.Z. Oener, A.M. Smith, L.J. Enman, K.E. Ayers, C. B. Capuano, J.N. Renner, N. Danilovic, Y. Li, H. Wang, Q. Zhang, S.W. Boettcher, ACS Catal. 9 (2019) 7–15, https://doi.org/10.1021/acscatal.8b04001.
[3] J. Rossmeisl, Z.W. Qu, H. Zhu, G.J. Kroes, J.K. Nørskov, J. Electroanal. Chem. 607 (1–2) (2007) 83–89, https://doi.org/10.1016/j.jelechem.2006.11.008.
[4] M.T.M. Koper, J. Electroanal. Chem. 660 (2) (2011) 254–260, https://doi.org/10.1016/j.jelechem.2010.10.004. ⟨http://www.sciencedirect.com/science/article/pii/S1572665710003917⟩.
[5] M.D. Merrill, R.C. Dougherty, J. Phys. Chem. C. 112 (10) (2008) 3655–3666, https://doi.org/10.1021/jp710675m.
[6] A. Singh, L. Spiccia, Coord. Chem. Rev. 257 (17) (2013) 2607–2622, https://doi.org/10.1016/j.ccr.2013.02.027. ⟨http://www.sciencedirect.com/science/article/pii/S0010854513000611⟩.
[7] L. Trotochaud, J.K. Ranney, K.N. Williams, S.W. Boettcher, J. Am. Chem. Soc. 134 (41) (2012) 17253–17261, https://doi.org/10.1021/ja307507a.
[8] H. Kato, K. Asakura, A. Kudo, J. Am. Chem. Soc. 125 (10) (2003) 3082–3089, https://doi.org/10.1021/ja027751g.
[9] Y. Wu, M. Chen, Y. Han, H. Luo, X. Su, M.-T. Zhang, X. Lin, J. Sun, L. Wang, L. Deng, W. Zhang, R. Cao, Angew. Chem. Int. Ed. 54 (16) (2015) 4870–4875, https://doi.org/10.1002/anie.201412389.
[10] T.Y. Ma, S. Dai, M. Jaroniec, S.Z. Qiao, Journal of the American Chemical Society, arXiv:arXiv:1408.1149 136 (39) (2014), https://doi.org/10.1021/ja5082553.

[11] R.D.L. Smith, M.S. Pre, R.D. Fagan, S. Trudel, M.S. Prévot, R.D. Fagan, S. Trudel, C. P. Berlinguette, J. Am. Chem. Soc. 135 (31) (2013) 11580–11586, https://doi.org/10.1021/ja403102j.

[12] J. Chi, H. Yu, G. Jiang, J. Jia, B. Qin, B. Yi, Z. Shao, J. Mater. Chem. A 6 (8) (2018) 3397–3401, https://doi.org/10.1039/c7ta10747a. ⟨http://xlink.rsc.org/?DOI=C7TA10747A⟩.

[13] L. Yu, H. Zhou, J. Sun, I.K. Mishra, D. Luo, F. Yu, Y. Yu, S. Chen, Z. Ren, J. Mater. Chem. A 6 (28) (2018) 13619–13623, https://doi.org/10.1039/C8TA02967A.

[14] D. Li, H. Liu, L. Feng, Energy Fuels 34 (11) (2020) 13491–13522, https://doi.org/10.1021/acs.energyfuels.0c03084.

[15] B.M. Hunter, W. Hieringer, J.R. Winkler, H.B. Gray, A.M. Müller, Energy Environ. Sci. 9 (5) (2016) 1734–1743, https://doi.org/10.1039/C6EE00377J. ⟨http://xlink.rsc.org/?DOI=C6EE00377J⟩.

[16] D.A. Corrigan, S.P. Maheswari, Electrochem. Soc. Ext. Abstr. 85–1 (1985) 934–935.

[17] D.A. Corrigan, R.M. Bendert, J. Electrochem. Soc. 136 (3) (1989) 723–728, https://doi.org/10.1149/1.2096717.

[18] L.J. Enman, M.S. Burke, A.S. Batchellor, S.W. Boettcher, ACS Catal. 6 (4) (2016) 2416–2423, https://doi.org/10.1021/acscatal.5b02924.

[19] X. Cui, B. Zhang, C. Zeng, H. Wen, S. Guo, Int. J. Hydrog. Energy 43 (32) (2018) 15234–15244, https://doi.org/10.1016/j.ijhydene.2018.06.109. ⟨https://www.sciencedirect.com/science/article/pii/S0360319918319815⟩.

[20] K. Xu, H. Ding, H. Lv, P. Chen, X. Lu, H. Cheng, T. Zhou, S. Liu, X. Wu, C. Wu, Y. Xie, Adv. Mater. 28 (17) (2016) 3326–3332, https://doi.org/10.1002/adma.201505732.

[21] M.B. Stevens, L.J. Enman, E.H. Korkus, J. Zaffran, C.D.M. Trang, J. Asbury, M. G. Kast, M.C. Toroker, S.W. Boettcher, M. Science, T. Nancy, S. Grand, T. Energy, P. Technion, Nano Res. 12 (2019) 2288–2295, https://doi.org/10.1007/s12274-019-2391-y.

[22] M. Tadic, D. Nikolic, M. Panjan, G.R. Blake, J. Alloy. Compd. 647 (2015) 1061–1068, https://doi.org/10.1016/j.jallcom.2015.06.027.

[23] J. FranciscoBorin, O. Baffa, Am. J. Phys. 66 (5) (1998) 449–452.

[24] S.P. Yeap, J. Lim, B.S. Ooi, A.L. Ahmad, J. Nanopart. Res. 19 (11) (2017) 368, https://doi.org/10.1007/s11051-017-4065-6.

[25] J.S. Andreu, J. Camacho, J. Faraudo, Soft Matter 7 (6) (2011) 2336–2339, https://doi.org/10.1039/C0SM01424A.

[26] P. Ganesan, A. Sivanantham, S. Shanmugam, J. Mater. Chem. A 4 (42) (2016) 16394–16402, https://doi.org/10.1039/C6TA04499A.

[27] C. Tang, H.-S. Wang, H.-F. Wang, Q. Zhang, G.-L. Tian, J.-Q. Nie, F. Wei, Adv. Mater. 27 (30) (2015) 4516–4522, https://doi.org/10.1002/adma.201501901.

[28] M. Chen, L. Wang, H. Yang, S. Zhao, H. Xu, G. Wu, J. Power Sources 375 (2018) 277–290, https://doi.org/10.1016/j.jpowsour.2017.08.062.

[29] I.S. Filimonenkov, S.Y. Istomin, E.V. Antipov, G.A. Tsirlina, E.R. Savinova, Electrochim. Acta 286 (2018) 304–312, https://doi.org/10.1016/j.electacta.2018.08.056.

[30] I.S. Filimonenkov, C. Bouillet, G. Kéranguéven, P.A. Simonov, G.A. Tsirlina, E. R. Savinova, Electrochim. Acta 321 (2019), https://doi.org/10.1016/j.electacta.2019.134657.

[31] I.S. Filimonenkov, G.A. Tsirlina, E.R. Savinova, Electrochim. Acta 319 (2019) 227–236, https://doi.org/10.1016/j.electacta.2019.06.154.

[32] W. Li, D. Xiong, X. Gao, L. Liu, Chem. Commun. 55 (60) (2019) 8744–8763, https://doi.org/10.1039/c9cc02845e.

[33] X. Yan, C.-L. Dong, Y.-C. Huang, Y. Jia, L. Zhang, S. Shen, J. Chen, X. Yao, Small Methods 3 (9) (2019), 1800439, https://doi.org/10.1002/smtd.201800439.

[34] X. Cui, P. Ren, D. Deng, J. Deng, X. Bao, Energy Environ. Sci. 9 (1) (2016) 123–129, https://doi.org/10.1039/C5EE03316K.

[35] S. Carenco, D. Portehault, C. Boissière, N. Mézailles, C. Sanchez, Adv. Mater. 26 (3) (2014) 371–390, https://doi.org/10.1002/adma.201303198.

[36] L. Peng, S.S.A. Shah, Z. Wei, Chin. J. Catal. 39 (10) (2018) 1575–1593, https://doi.org/10.1016/S1872-2067(18)63130-4. ⟨http://www.sciencedirect.com/science/article/pii/S1872206718631304⟩.

[37] M. Plevová, J. Hnát, K. Bouzek, 9, J. Power Sources 507 (2021), https://doi.org/10.1016/j.jpowsour.2021.230072, 9.

[38] B.R. Wygant, K. Kawashima, C.B. Mullins, ACS Energy Lett. 3 (12) (2018) 2956–2966, https://doi.org/10.1021/acsenergylett.8b01774.

[39] P.F. Liu, X. Li, S. Yang, M.Y. Zu, P. Liu, B. Zhang, L.R. Zheng, H. Zhao, H.G. Yang, ACS Energy Lett. 2 (10) (2017) 2257–2263, https://doi.org/10.1021/acsenergylett.7b00638.

[40] H. Liang, A.N. Gandi, C. Xia, M.N. Hedhili, D.H. Anjum, U. Schwingenschlögl, H. N. Alshareef, ACS Energy Lett. 2 (5) (2017) 1035–1042, https://doi.org/10.1021/acsenergylett.7b00206.

[41] X. Wang, W. Li, D. Xiong, D.Y. Petrovykh, L. Liu, Adv. Funct. Mater. 26 (23) (2016) 4067–4077, https://doi.org/10.1002/adfm.201505509.

[42] X. Wang, W. Li, D. Xiong, L. Liu, J. Mater. Chem. A 4 (15) (2016) 5639–5646, https://doi.org/10.1039/C5TA10317G.

[43] W. Li, X. Gao, X. Wang, D. Xiong, P.-P. Huang, W.-G. Song, X. Bao, L. Liu, J. Power Sources 330 (2016) 156–166, https://doi.org/10.1016/j.jpowsour.2016.08.126.

[44] W. Li, X. Gao, D. Xiong, F. Xia, J. Liu, W.-G. Song, J. Xu, S.M. Thalluri, M. F. Cerqueira, X. Fu, L. Liu, Chem. Sci. 8 (4) (2017) 2952–2958, https://doi.org/10.1039/c6sc05167g.

[45] H. Khani, N.S. Grundish, D.O. Wipf, J.B. Goodenough, Adv. Energy Mater. 10 (1) (2020), 1903215, https://doi.org/10.1002/aenm.201903215.

[46] Y. Zhou, H. Liu, X. Gu, X. Wu, L. Feng (January), Carbon Energy (2022), https://doi.org/10.1002/cey2.206 (January).

[47] J.H. Jang, A.A. Jeffery, J. Min, N. Jung, S.J. Yoo, Nanoscale 13 (36) (2021) 15116–15141, https://doi.org/10.1039/d1nr01328a.

[48] X. Chen, J. Xiao, J. Wang, D. Deng, Y. Hu, J. Zhou, L. Yu, T. Heine, X. Pan, X. Bao, Chem. Sci. 6 (5) (2015) 3262–3267, https://doi.org/10.1039/C5SC00353A.

[49] L. Zhang, J. Xiao, H. Wang, M. Shao, ACS Catal. 7 (11) (2017) 7855–7865, https://doi.org/10.1021/acscatal.7b02718.

[50] S. Carenco, C. Surcin, M. Morcrette, D. Larcher, N. Mézailles, C. Boissière, C. Sanchez, Chem. Mater. 24 (4) (2012) 688–697, https://doi.org/10.1021/cm203164a.

[51] M. Sharma, N. Jung, S.J. Yoo, Chem. Mater. 30 (1) (2018) 2–24, https://doi.org/10.1021/acs.chemmater.7b03422.

[52] E. Muthuswamy, G.H. Layan Savithra, S.L. Brock, ACS Nano 5 (3) (2011) 2402–2411, https://doi.org/10.1021/nn1033357.

[53] S. Trasatti, O. Petrii, Pure Appl. Chem. 63 (5) (1991) 711–734.

[54] C.C.L. McCrory, S. Jung, I.M. Ferrer, S.M. Chatman, J.C. Peters, T.F. Jaramillo, J. Am. Chem. Soc. 137 (13) (2015) 4347–4357, https://doi.org/10.1021/ja510442p.

[55] C.C.L. McCrory, S. Jung, J.C. Peters, T.F. Jaramillo, J. Am. Chem. Soc. 135 (45) (2013) 16977–16987, https://doi.org/10.1021/ja407115p.

[56] E. Kuznetsova, A. Cuesta, M.S. Thomassen, S. Sunde, J. Electroanal. Chem. 728 (2014) 102–111, https://doi.org/10.1016/j.jelechem.2014.06.031.

[57] P. Chen, L.-K. Wang, G. Wang, M.-R. Gao, J. Ge, W.-J. Yuan, Y.-H. Shen, A.-J. Xie, S.-H. Yu, Energy Environ. Sci. 7 (12) (2014) 4095–4103, https://doi.org/10.1039/C4EE02531H.

[58] A. Hitihami-Mudiyanselage, M.P. Arachchige, T. Seda, G. Lawes, S.L. Brock, Chem. Mater. 27 (19) (2015) 6592–6600, https://doi.org/10.1021/acs.chemmater.5b02149.

[59] A.F. Gaudette, A.W. Burns, J.R. Hayes, M.C. Smith, R.H. Bowker, T. Seda, M. E. Bussell, J. Catal. 272 (1) (2010) 18–27, https://doi.org/10.1016/j.jcat.2010.03.016.

[60] S. Surendran, S. Shanmugapriya, S. Shanmugam, L. Vasylechko, R. KalaiSelvan, ACS Appl. Energy Mater. 1 (1) (2018) 78–92, https://doi.org/10.1021/acsaem.7b00006.

[61] J.B. Goodenough, J. Solid State Chem. 7 (4) (1973) 428–447, https://doi.org/10.1016/0022-4596(73)90172-2. ⟨https://www.sciencedirect.com/science/article/pii/0022459673901722⟩.

[62] P.E.R. Blanchard, A.P. Grosvenor, R.G. Cavell, A. Mar, J. Mater. Chem. 19 (33) (2009) 6015–6022, https://doi.org/10.1039/B904250D.

[63] D.S. Hall, D.J. Lockwood, C. Bock, B.R. MacDougall, Proc. R. Soc. A: Math., Phys. Eng. Sci. 471 (2174) (2015), https://doi.org/10.1098/rspa.2014.0792.

[64] B. Sriram, J.N. Baby, S.F. Wang, R. Ranjitha M, M. Govindasamy, M. George, ACS Sustain. Chem. Eng. 8 (48) (2020) 17772–17782, https://doi.org/10.1021/acssuschemeng.0c06070.

[65] H. Li, H. Li, W.-L. Dai, W. Wang, Z. Fang, J.-F. Deng, Appl. Surf. Sci. 152 (1) (1999) 25–34, https://doi.org/10.1016/S0169-4332(99)00294-9. ⟨http://www.sciencedirect.com/science/article/pii/S0169433299002949⟩.

[66] P.E.R. Blanchard, A.P. Grosvenor, R.G. Cavell, A. Mar, Chem. Mater. 20 (22) (2008) 7081–7088, https://doi.org/10.1021/cm802123a.

[67] Z. Yu, J. Xu, I. Amorim, Y. Li, L. Liu, J. Energy Chem. 58 (2021) 256–263, https://doi.org/10.1016/j.jechem.2020.10.016.

[68] F. D'Accriscio, E. Schrader, C. Sassoye, M. Selmane, R.F. André, S. Lamaison, D. Wakerley, M. Fontecave, V. Mougel, G.Le Corre, et al., ChemNanoMat 6 (8) (2020) 1208–1219.

[69] S. Carenco, D. Portehault, C. Boissière, N. Mézailles, C. Sanchez, Chem. Rev. 113 (10) (2013) 7981–8065, https://doi.org/10.1021/cr400020d.

[70] F. D'Accriscio, E. Schrader, C. Sassoye, M. Selmane, R.F. André, S. Lamaison, D. Wakerley, M. Fontecave, V. Mougel, G. LeCorre, H. Grützmacher, C. Sanchez, S. Carenco, ChemNanoMat 6 (8) (2020) 1208–1219, https://doi.org/10.1002/cnma.202000198.

[71] Z. Huang, Z. Chen, Z. Chen, C. Lv, H. Meng, C. Zhang, ACS Nano 8 (8) (2014) 8121–8129, https://doi.org/10.1021/nn5022204.

[72] S. Klaus, Y. Cai, M.W. Louie, L. Trotochaud, A.T. Bell, J. Phys. Chem. C. 119 (13) (2015) 7243–7254, https://doi.org/10.1021/acs.jpcc.5b00105.

[73] M.B. Stevens, C.D. Trang, L.J. Enman, J. Deng, S.W. Boettcher, J. Am. Chem. Soc. 139 (33) (2017) 11361–11364, https://doi.org/10.1021/jacs.7b07117.

[74] F. Dionigi, P. Strasser, Adv. Energy Mater. 6 (23) (2016), https://doi.org/10.1002/aenm.201600621.

[75] M. Görlin, P. Chernev, J.F. De Araújo, T. Reier, S. Dresp, B. Paul, R. Krähnert, H. Dau, P. Strasser, arXiv:arXiv:1408.1149, J. Am. Chem. Soc. 138 (17) (2016) 5603–5614, https://doi.org/10.1021/jacs.6b00332.

[76] D.F. Abbott, E. Fabbri, M. Borlaf, F. Bozza, R. Schaeublin, M. Nachtegaal, T. Graule, T.J. Schmidt, J. Mater. Chem. A 6 (47) (2018) 24534–24549, https://doi.org/10.1039/c8ta09336a.

[77] A.H. Reksten, H. Thuv, F. Seland, S. Sunde (July 2017), J. Electroanal. Chem. 819 (2018) 547–561, https://doi.org/10.1016/j.jelechem.2018.04.018.

[78] A. Damjanovic, A. Dey, J. Bockris, Electrochim. Acta 11 (7) (1966) 791–814, https://doi.org/10.1016/0013-4686(66)87056-1. ⟨http://www.sciencedirect.com/science/article/pii/0013468666870561⟩.

[79] A. Damjanovic, M. Genshaw, J. Bockris, J. Electrochem. Soc. 114 (5) (1967) 466.

[80] R. Doyle, M. Lyons, J. Electrochem. Soc. 160 (2) (2013) H142.

[81] J.O. Bockris, T. Otagawa, J. Phys. Chem. 87 (15) (1983) 2960–2971, https://doi.org/10.1021/j100238a048.

[82] J.O. Bockris, J. Electrochem. Soc. 131 (2) (1984) 290, https://doi.org/10.1149/1.2115565.

[83] F. Jaouen, G. Lindbergh, J. Electrochem. Soc. 150 (12) (2003) A1699.

[84] M. Darab, A.O. Barnett, G. Lindbergh, M.S. Thomassen, S. Sunde, Electrochim. Acta 232 (2017) 505–516, https://doi.org/10.1016/j.electacta.2017.02.101. ⟨https://www.sciencedirect.com/science/article/pii/S0013468617303778⟩.

[85] S.L. daSilva, E.A. Ticianelli, J. Electroanal. Chem. 391 (1–2) (1995) 101–109.
[86] J. Kibsgaard, I. Chorkendorff (June), Nat. Energy 4 (2019), https://doi.org/10.1038/s41560-019-0407-1 (June).
[87] S. Carenco, S. Labouille, S. Bouchonnet, C. Boissière, X.F. LeGoff, C. Sanchez, N. Mézailles, Chem. - A Eur. J. 18 (44) (2012) 14165–14173, https://doi.org/10.1002/chem.201201071.
[88] R.L. McCreery, Chem. Rev. 108 (7) (2008) 2646–2687, https://doi.org/10.1021/cr068076m.
[89] J. Li, S. Ghoshal, W. Liang, M.-T. Sougrati, F. Jaouen, B. Halevi, S. McKinney, G. McCool, C. Ma, X. Yuan, Z.-F. Ma, S. Mukerjee, Q. Jia, ENERGY Environ. Sci. 9 (7) (2016) 2418–2432, https://doi.org/10.1039/c6ee01160h.
[90] M. Toebes, J. Bitter, A. van Dillen, K. de Jong, 5th European Congress on Catalysis (EuropaCat 5), Limerick, Ireland, SEP, 2001, Catal. Today 76 (1) (2002) 33–42, https://doi.org/10.1016/S0920-5861(02)00209-2.
[91] L. Yan, H. Jiang, Y. Wang, L. Li, X. Gu, P. Dai, D. Liu, S.-f. Tang, G. Zhao, X. Zhao, K.M. Thomas, Electrochim. Acta 297 (2019) 755–766, https://doi.org/10.1016/j.electacta.2018.12.020.
[92] Y. Yao, N. Mahmood, L. Pan, G. Shen, R. Zhang, R. Gao, F.E. Aleem, X. Yuan, X. Zhang, J.J. Zou, Nanoscale 10 (45) (2018) 21327–21334, https://doi.org/10.1039/c8nr06752j.